

Inner core heterogeneity induced by a large variation in lower mantle heat flux

Aditya Varma, Binod Sreenivasan

Centre for Earth Sciences, Indian Institute of Science, Bangalore 560012, India

Abstract

Seismic mapping of the top of the inner core indicates two distinct areas of high P-wave velocity, the stronger one located beneath Asia, and the other located beneath the Atlantic. This two-fold pattern supports the idea that a lower-mantle heterogeneity can be transmitted to the inner core through outer core convection. In this study, a two-component convective dynamo model, where thermal convection is near critical and compositional convection is strongly supercritical, produces a substantial inner core heterogeneity in the rapidly rotating strongly driven regime of Earth's core. While the temperature profile that models secular cooling ensures that the mantle heterogeneity propagates as far as the inner core boundary (ICB), the distribution of heat flux at the ICB is determined by the strength of compositional buoyancy. A large heat flux variation q^* of $O(10)$ at the core–mantle boundary (CMB), where q^* is the ratio of the maximum heat flux difference to the mean heat flux at the CMB, produces a core flow regime of long-lived convection in the east and time-varying convection in the west. Here, the P-wave velocity estimated from the ICB heat flux in the dynamo is higher in the east than in the west, with the hemispherical difference of the same order as the observed lower bound, 0.5 %. Additional observational constraints are satisfied in this regime – the variability of high-latitude magnetic flux in the east is lower than that in the west; and the stratified F-layer at the base of the outer core, which is fed by the mass flux from regional melting of the inner core and magnetically damped, attains a steady-state height of ~ 200 km.

1. Introduction

Seismic tomography of the lower mantle indicates regions of high shear wave velocity beneath Asia and the Atlantic and low velocity beneath the Pacific and Africa (e.g Masters et al., 2000). While the fast regions cause preferential cooling of the outer core, the slow regions inhibit core convection. The high-latitude lobes of magnetic flux beneath Asia and America and the weak secular variation in the Pacific point to the effect of the approximately two-fold pattern of lower-mantle heterogeneity on the geodynamo (Willis et al., 2007). Since the heat flux variation at the core–mantle boundary (CMB) is not likely to have changed much in the past ~ 200 Myr (Torsvik et al., 2006), the evolution of the geodynamo subject to a quasi-stationary lateral variation in lower-mantle heat flux is reproduced by numerical dynamo simulations (e.g. Takahashi et al., 2008; Olson and Amit, 2015; Mound and Davies, 2023). Although a simplified two-fold pattern of convection in the core is often used to explain the non-axisymmetry of the magnetic field induced by the mantle, a large variation in CMB heat flux (Olson et al., 2018; Mound et al., 2019) gives rise to a substantial east–west dichotomy in the core flow (Sahoo and Sreenivasan, 2020a), consisting of coherent (long-lived) convection beneath Asia and time-varying convection beneath America. If this pattern of convection in turn causes a heterogeneity at the inner core boundary (ICB), then a measure of this heterogeneity would place a constraint on the magnitude of the heat flux variation at the CMB.

Seismic mapping of the top of the inner core indicates an east–west lateral heterogeneity, with the East having a higher isotropic velocity than the West. The differences in the isotropic P-wave velocity v_p at the top of the inner core lie between 0.5% and 1.5% (Tanaka and Hamaguchi, 1997; Niu and Wen, 2001; Sun and Song, 2008; Waszek and Deuss, 2011). Isotropy, in this context, means that the wave speeds are the same in all directions. Later studies suggest a more complex velocity structure, with the east–west variation showing a dominant two-fold (wavenumber $m = 2$) pattern (Cormier and Attanayake, 2013; Tkalčić et al., 2024) – there are two distinct areas of high velocity in the upper inner core, the stronger one located beneath Asia, and the other located beneath the Atlantic. This pattern

lends credence to the idea that a large lower-mantle heterogeneity can be transmitted to the inner core via outer core convection.

Numerical dynamo simulations that study the influence of the laterally varying lower-mantle heat flux on the geodynamo suggest that a cyclonic vortex beneath Asia causes a hemispherical variation in the freezing rate of the inner core, with the eastern hemisphere freezing faster than the western hemisphere (Aubert et al., 2008; Gubbins et al., 2011). In addition, models that simulate secular cooling of the core through volumetric heat sources produce areas of reversed (inward) heat flux at the ICB, indicating possible melting of the inner core (Gubbins et al., 2011). Laboratory models of the core where convection onsets in close proximity to the imposed lateral variation (Sahoo and Sreenivasan, 2020b) also produce heat flux reversals at the ICB. In contrast, basally heated numerical models operating in the strongly forced regime of present-day Earth (Sreenivasan and Gubbins, 2008) swamp any influence of the CMB heat flux anomalies, which might lead one to infer that the CMB anomalies do not reach the ICB (Davies and Mound, 2019). It may be noted that similar models, where the maximum heat flux variation at the CMB is ~ 5 times the mean heat flux (Sahoo and Sreenivasan, 2020a; Mound and Davies, 2023), reproduce the high-latitude magnetic flux in the present-day field well. To satisfy the observational constraints placed by the field as well as the heterogeneity of the ICB, the present study considers a two-component convective dynamo model. Here, the strong compositional buoyancy ensures the east–west variation of the observed field while the relatively weak thermal buoyancy that mimics secular cooling ensures that the mantle-induced anomalies not only reach the ICB but also provide a measurable estimate of the seismic velocity difference at the top of the inner core.

Seismic observations suggest the presence of a low- ν_p layer at the base of the outer core. This stably stratified ‘F-layer’ (Souriau and Poupinet, 1991; Gubbins et al., 2008) may form from the lateral spread of melt originating from the regions of inward heat flux at the ICB. By varying the lower-mantle heat flux variation q^* in the range ~ 1 –10 in dynamo models, where q^* is the ratio of the maximum heat flux variation to the mean heat flux at

the CMB, the lowest q^* at which heat flux reverses at the ICB may be found. Similar to the pattern of inner core freezing, we anticipate a two-fold pattern for melting, with an area beneath the Pacific being more dominant than that beneath Africa. The height of the F-layer at the equator is a function of the mean hemispherical heat flux and the axial (z) field intensity in the dynamo. The present study aims to show that the F-layer heights predicted by observations can be realized by inner core heat flux variations induced by lower-mantle variations of q^* $O(10)$.

The paper is organized as follows. In Section 2, the dynamo model and the core flows that would produce the heat flux heterogeneity at the ICB are discussed. Based on the east–west differences in the heat flux measured in the dynamo simulations, estimates are obtained for the hemispherical differences in inner core freezing rate and P-wave velocity, the comparison of which with seismic observations would place a lower bound on q^* . In addition, the simulations provide an estimate of the height of stratified F-layer thought to be fed by regional melting of the inner core, which also affords comparisons with predictions based on observations. Further, the longitudinal variation of the high-latitude flux lobes in the high- q^* simulations are compared with that of the present-day field. Section 3 gives the implications of this study for the Earth’s core.

2. Inner core heterogeneity in a two-component convective dynamo model

2.1. The dynamo model

We consider dynamo action in a rotating, electrically conducting fluid confined between two concentric, co-rotating spherical surfaces that correspond to the ICB and the CMB. The ratio of inner to outer radius, r_i/r_o , is chosen to be 0.35. To obtain the non-dimensional governing equations, lengths are scaled by the thickness of the spherical shell L , time is scaled by the magnetic diffusion time, L^2/η , where η is the magnetic diffusivity, the velocity field u is scaled by η/L , and the magnetic field B is scaled by $(2\Omega\mu\eta\rho)^{1/2}$ where Ω is the rotation rate, ρ is the fluid density, and μ is the magnetic permeability. The temperature T is scaled by $\beta_T L$, where β_T is the mean heat flux at the CMB, and the composition

C is scaled by $\beta_C L$, where β_C is the mean composition flux at the ICB.

The governing equations for \mathbf{u} , \mathbf{B} , T and C are given by

$$EPm^{-1} \left(\frac{\partial \mathbf{u}}{\partial t} + (\nabla \times \mathbf{u}) \times \mathbf{u} \right) + \hat{\mathbf{z}} \times \mathbf{u} = -\nabla p^* + PmPr^{-1} ERa^T T \mathbf{r} \\ + PmSc^{-1} ERa^C C \mathbf{r} + (\nabla \times \mathbf{B}) \times \mathbf{B} + E \nabla^2 \mathbf{u}, \quad (1)$$

$$\frac{\partial \mathbf{B}}{\partial t} = \nabla \times (\mathbf{u} \times \mathbf{B}) + \nabla^2 \mathbf{B}, \quad (2)$$

$$\frac{\partial T}{\partial t} + (\mathbf{u} \cdot \nabla) T = PmPr^{-1} \nabla^2 T + S_o, \quad (3)$$

$$\frac{\partial C}{\partial t} + (\mathbf{u} \cdot \nabla) C = PmSc^{-1} \nabla^2 C + S_i, \quad (4)$$

$$\nabla \cdot \mathbf{u} = \nabla \cdot \mathbf{B} = 0, \quad (5)$$

where the modified pressure p^* is given by $p + \frac{1}{2} EPm^{-1} |\mathbf{u}^2|$. The dimensionless parameters in the equations (1)–(5) are the Ekman number $E = \nu / 2\Omega L^2$, the Prandtl number, $Pr = \nu / \kappa_T$, Schmidt number, $Sc = \nu / \kappa_C$, the magnetic Prandtl number, $Pm = \nu / \eta$, the thermal Rayleigh number $Ra^T = g\alpha\beta_T L^4 / \nu\kappa_T$, the compositional Rayleigh number $Ra^C = g\alpha\beta_C L^4 / \nu\kappa_C$. Here, g is the gravitational acceleration, ν is the kinematic viscosity, κ_T is the thermal diffusivity, κ_C is the compositional diffusivity, and α is the coefficient of thermal expansion.

The velocity and magnetic fields satisfy the no-slip and electrically insulating conditions, respectively. The basic state temperature profile represents an internal heating with a source S_o , which models secular cooling (Willis et al., 2007). An isothermal condition is set at the ICB and a fixed heat flux condition at the CMB. The pattern of heat flux at the CMB is derived from the seismic shear wave velocity variation in the lower mantle (Masters et al., 2000; Sahoo and Sreenivasan, 2020a). The compositional profile uses a uniform volumetric sink S_i (e.g. Manglik et al., 2010) with a constant flux at the ICB and zero flux at the CMB. The basic state profiles of the temperature and the compositional gradient are given by

$$T_0 = \frac{Pr}{Pm} \frac{S_o}{6} (r_i^2 - r^2), \quad \frac{\partial C_0}{\partial r} = \frac{Sc}{Pm} \frac{S_i}{3} \left(\frac{r_o^3}{r^2} - r \right). \quad (6a,b)$$

The fixed parameters used in the simulations are $Pr = 0.1$, $Sc = 1$ and $Pm = 1$. The scaled magnetic field \bar{B} is an output derived from our dynamo simulations as a root mean square (rms) value, where the mean is a volume average. The input and output parameters of the simulations are given in table 1. The calculations are performed by a code that uses spherical harmonic expansions in the angular coordinates (θ, ϕ) and finite differences in radius r (e.g. Willis et al., 2007).

S. No.	E	q^*	Ra^T ($\times 10^6$)	Ra^C ($\times 10^9$)	Ra^C/Ra_{cr}^C	N_r	l	\bar{B}	Rm	Ro_l
a	2×10^{-6}	1	7.2	2	129	240	260	1.74	567	0.010
b		2	6.75	2	129	256	260	1.68	543	0.012
c		7	5.75	1	65	192	192	1.22	251	0.007
d		7	5.75	1.5	97	192	230	1.47	405	0.010
e		7	5.75	2	129	240	260	1.65	525	0.012
f		7	5.75	2.75	177	240	288	1.95	632	0.018
g		10	4.3	2.75	177	256	270	2.05	588	0.014
h		10	4.3	3.50	225	256	288	2.22	611	0.017
i		10	4.3	4.35	275	240	288	2.41	652	0.022
j	1×10^{-5}	10	1.12	0.90	360	144	144	2.26	372	0.023
k		15	0.9	1.05	420	144	160	2.47	410	0.029

Table 1: Parameters of dynamo simulations in this study. Here, N_r is the number of radial points, l is the spherical harmonic degree, \bar{B} is the volume-averaged magnetic field, Rm is the magnetic Reynolds number, Ro_l is the local Rossby number, E is the Ekman number, Ra^T is the thermal Rayleigh number, Ra^C is the compositional Rayleigh number and q^* is the dimensionless measure of the heat flux heterogeneity at the outer boundary. The common dimensionless parameters are $Pr = 0.1$, $Sc = 1$, $Pm = 1$.

2.2. Outer core flow and ICB heat flux

In the simulations, the thermal Rayleigh number Ra^T is set to critical while the compositional Rayleigh number Ra^C is varied and is kept highly supercritical, consistent with the respective estimates of Ra/Ra_{cr} for nonmagnetic convection with turbulent diffusivities (e.g. Gubbins, 2001). The measure of lateral heterogeneity at the CMB, defined by q^* in Section 1, ranges from 1 to 15 in the simulations (table 1).

We examine the core flow and ICB heat flux distribution for varying q^* and Ra^C . The equatorial section and cylindrical surface plots of the radial velocity u_r are given in figure 1. The (z, ϕ) surface plots at cylindrical radius $s = 1.2$, shown in figure 1 (d)-(f), indicate that the columnar structure of the downwelling is preserved even at large q^* . Therefore, the dynamo operates in a rapidly rotating regime that generates a strong field of volume-averaged intensity $\bar{B} = O(1)$. For $Ra^C \approx 65 \times Ra_{cr}^C$ and $q^* = 7$, the convective downwelling beneath America is dominant while the downwelling beneath Asia is not well developed (figure 1 (a) and (d)). This hemispherical dichotomy, found only at large q^* , has its origins in the onset of convection beneath the seismically faster region in the West (Sahoo and Sreenivasan, 2020a). As Ra^C is increased to $\approx 100 \times Ra_{cr}^C$, coherent (long-lived) downwellings exist beneath both Asia and America (figures 1(b) and (e)), reminiscent of the convection pattern obtained with a Y_2^2 heat flux variation at the CMB (Willis et al., 2007). For a stronger forcing of $Ra^C \approx 130 \times Ra_{cr}^C$, the downwelling beneath America disintegrates and gives way to a time-varying cluster of rolls while the downwelling beneath Asia remains long-lived (figures 1(c) and (f)). The enhanced compositional convection beneath Asia might produce a thin low P-wave velocity layer overlying a high-velocity, fast-freezing region (Cormier et al., 2021, p. 203). This core flow regime is likely Earth-like as it produces high-latitude magnetic flux lobes which are more unstable in the West than in the East in the historical period of direct observation (Jackson et al., 2000; Gubbins et al., 2007).

The effect of inhomogeneous outer core convection on the freezing rate of the inner core is understood by plotting the heat flux distribution on the ICB in the dynamo (figure 2). Here, positive values indicate radially outward heat flux while negative values give radially

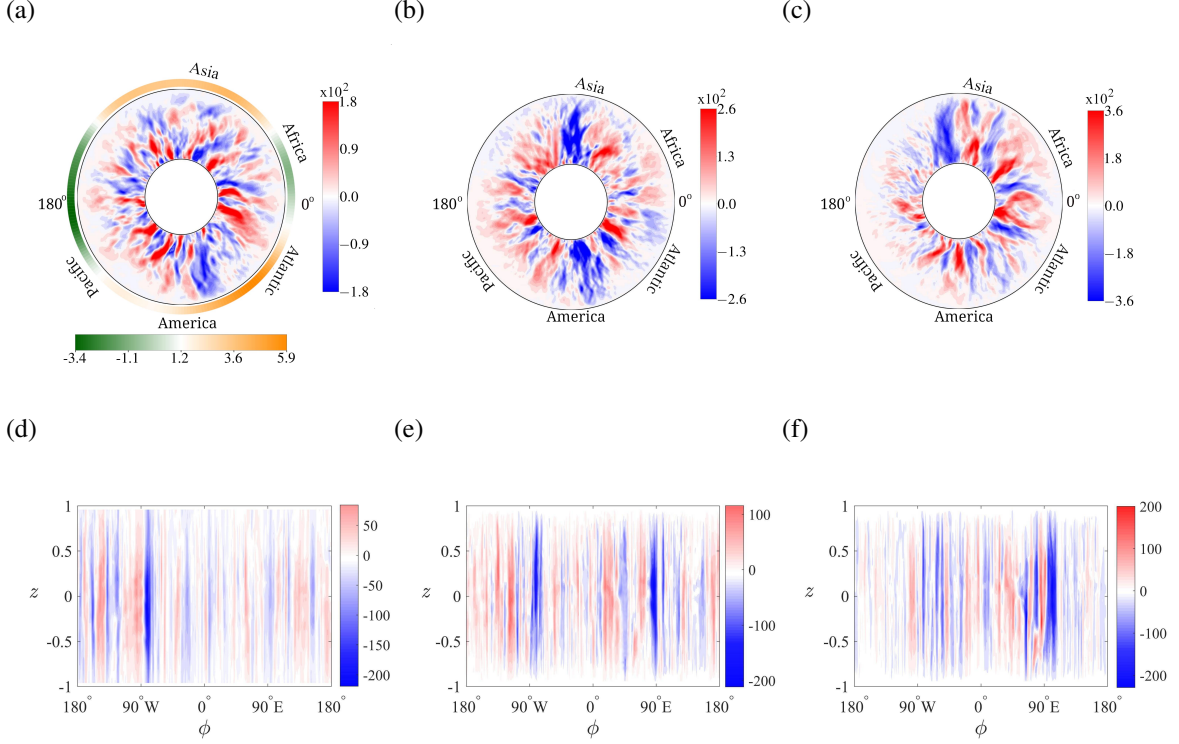


Figure 1: Radial velocity (u_r) at the equator (a–c) and a cylindrical surface of radius $s = 0.8r_o$ (d–f) for varying Ra^C in dynamo simulations. (a) and (d) $Ra^C = 1 \times 10^9$, (b) and (e) $Ra^C = 1.5 \times 10^9$, (c) and (f) $Ra^C = 2 \times 10^9$. A fixed CMB heterogeneity of $q^* = 7$ is used in all simulations. The common parameters in the simulations are $Ra^T = 5.75 \times 10^6$, $Pr = 0.1$, $Sc = 1$, $Pm = 1$, and $E = 2 \times 10^{-6}$. The plots are averaged over 10 turnover times.

inward heat flux. The line plots in figure 2 (b,d,f) show the variation of ICB heat flux (Q_{ic}) at the equator (blue line) and 30°S (red line). The variation in heat flux is largely confined to the region between these latitudes, and closely follows the pattern of convection in figure 1. The highest positive heat flux occurs approximately where the coherent downwelling impinges on the ICB. The regions of positive heat flux are separated by troughs of negative (inward) heat flux at the equator beneath Africa and the Pacific. When equally coherent downwellings exist beneath Asia and America (figure 1 (b)), the peak positive heat flux on the ICB equator is nearly equal in both hemispheres but the negative heat flux is more pronounced beneath the Pacific than Africa (figure 2 (d)). The core flow regime with a

coherent downwelling beneath Asia and time-varying convection beneath America (figure 1 (c)) produces peak positive ICB heat flux between 80°E and 100°E . The heat flux pattern may be considered to be the superposition of a hemispherical ($m = 1$) variation on an underlying, predominantly two-fold ($m = 2$) variation.

In all flow regimes, the greatest variation in ICB heat flux occurs in the equatorial region. Inward heat flux is not present beyond 30°S and 30°N , and the azimuthal variation at higher latitudes is much smaller than that at low latitudes. As the regime with quasi-stationary convection beneath Asia and time-varying convection beneath America is relevant to present-day Earth, it is examined in detail below.

Figure 3 (a) shows the ICB heat flux distribution in dynamos driven by one-component convection using basal heating and a uniform volumetric heat sink (see Appendix A for the model description). This buoyancy profile is known to promote boundary effects on the convection even in strong forcing (Sreenivasan and Gubbins, 2008). Here, the CMB anomalies do not reach the ICB even at $q^* = 10$, in agreement with strongly forced basally heated models (Davies and Mound, 2019). In contrast, the dynamos driven by two-component convection consistently show the mantle-induced heterogeneity of the inner core (figure 3 b–d). The peak ICB heat flux for most simulations is located within 80°E – 100°E , which is in good agreement with the location of peak P-wave velocities in Cormier and Attanayake (2013). Regions of higher positive heat flux freeze faster, leading to higher isotropic P-wave velocities. Cormier and Attanayake (2013) also obtain a local peak beneath the Atlantic, which corresponds to the location of preferred convection in the Western hemisphere. In general, there are two regions of high positive heat flux beneath Asia and America and two regions of low or negative heat flux beneath Africa and the Pacific.

Simulations with q^* of $O(1)$ and $O(10)$ present marked differences in the ICB heat flux pattern. For $q^* = 1$ and $q^* = 2$ (figure 3 (b)), difference in positive heat flux between the two hemispheres is small; furthermore, the heat flux does not reverse in sign. For q^* of $O(10)$, the positive heat flux beneath Asia is systematically higher than that beneath

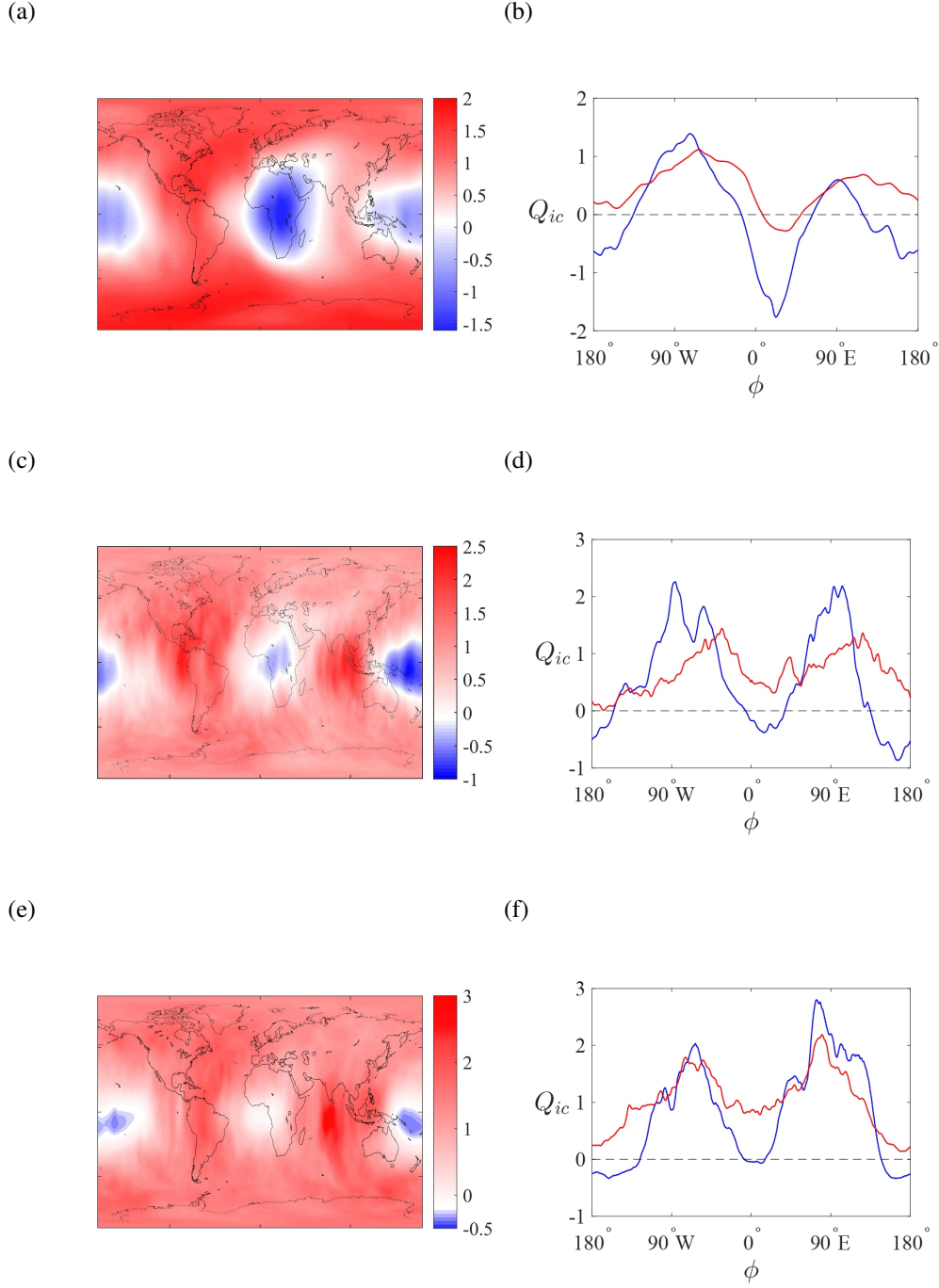


Figure 2: ICB heat flux distribution (left panels) and longitudinal variation of the ICB heat flux (right panels) at the equator (blue line) and at 30°S (red line), for varying Ra^C at a fixed CMB heterogeneity $q^* = 7$ in dynamo simulations. (a) and (b) $Ra^C = 1 \times 10^9$, (c) and (d) $Ra^C = 1.5 \times 10^9$, (e) and (f) $Ra^C = 2 \times 10^9$. The common parameters in the simulations are $Ra^T = 5.75 \times 10^7$, $Pr = 0.1$, $Sc = 1$, $Pm = 1$, and $E = 2 \times 10^{-6}$. The dashed horizontal lines correspond to zero heat flux. The plots are averaged over 10 turnover times.

America; furthermore, the reversal of heat flux is observed dominantly beneath the Pacific (figure 3 (c)). The increased negative heat flux under the Pacific plays a significant role in the east–west dichotomy. The region beneath Africa experiences only a marginally negative heat flux although its magnitude might increase at still higher q^* .

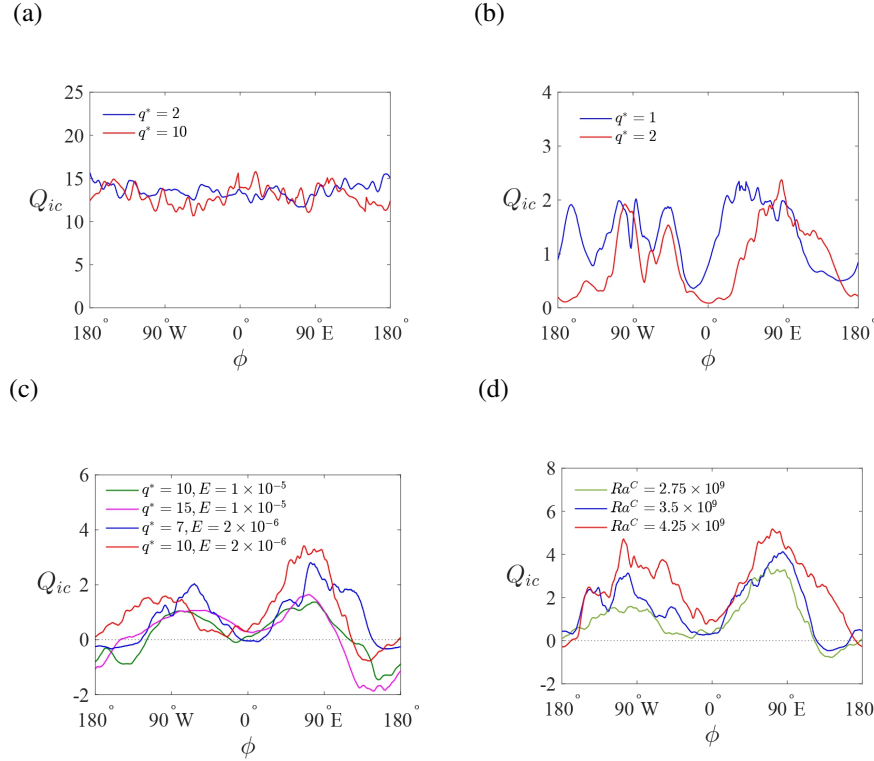


Figure 3: (a): Heat flux measured at the equator of the ICB (Q_{ic}) for two values of q^* in the dynamos driven by one-component convection with parameters $Ra = 2 \times 10^9$, $Pr = 1$, $Pm = 1$, $E = 2 \times 10^{-6}$ (Appendix A). (b)–(d) Heat flux measured at the equator of the ICB in the two-component convective dynamos for different values of q^* in the regime of coherent convection beneath Asia and time-varying convection beneath America. The parameters not given in the legends are (b) blue - $Ra^T = 7.2 \times 10^6$, $Ra^C = 2 \times 10^9$, $E = 2 \times 10^{-6}$; red - $Ra^T = 6.75 \times 10^6$, $Ra^C = 2 \times 10^9$, $E = 2 \times 10^{-6}$, (c) blue - $Ra^T = 5.75 \times 10^6$, $Ra^C = 2 \times 10^9$; red - $Ra^T = 4.3 \times 10^6$, $Ra^C = 2.75 \times 10^9$; green - $Ra^T = 1.12 \times 10^6$, $Ra^C = 0.9 \times 10^9$; magenta - $Ra^T = 0.9 \times 10^6$, $Ra^C = 1.05 \times 10^9$, (d) $Ra^T = 4.3 \times 10^6$, $E = 2 \times 10^{-6}$, $q^* = 10$ for all three runs. The thermal Rayleigh number Ra^T is kept at its critical value for nonmagnetic convection in all simulations. The common parameters are $Pr = 0.1$, $Sc = 1$ and $Pm = 1$. The horizontal dotted black lines in (c) and (d) show zero heat flux. The plots are averaged for 10 turnover times.

The effect of progressively increasing Ra^C at a given q^* on the ICB heat flux is given in figure 3 (d). Increasing Ra^C causes the positive heat flux to increase overall, resulting in a higher average heat flux. The negative heat flux beneath Africa and the Pacific is reduced as a result. The difference in average heat flux between the eastern and western hemispheres reduces as Ra^C is increased.

2.3. East-West differences in freezing rate and seismic velocity

The differences in heat flux between the eastern and western hemispheres manifest as variations in freezing rates and P-wave speeds within the upper 100 km of the inner core (Niu and Wen, 2001). To estimate these variations, we focus on the ICB region between 30°S and 30°N . These latitudinal bounds are chosen because they encompass the regions of enhanced and reversed heat flux observed at the ICB. The high latitudes exhibit little lateral variation and it is unlikely that high q^* accompanied by high Ra^C would widen the range of latitudes of ICB heterogeneity. The choice of the latitudinal bands is also justified by seismic studies (e.g. Ohtaki et al., 2012), where the highest compressional velocity is confined to equatorial East Asia. This is broadly consistent with the location of the peak heat flux in our dynamo simulations.

To obtain the average density at the top of the inner core in the eastern and western hemispheres, ρ_e and ρ_w , one must first estimate the mass fractions of solid and liquid iron, x_s and x_l respectively, in either hemisphere, which is in turn determined by the ICB heat flux measured in the dynamo. The solid mass fraction in the east, $x_{s,e}$, is first estimated as follows. The solid mass fraction at any point is taken to be unity for heat flux $Q \geq \bar{Q}_{ic}$, where \bar{Q}_{ic} is the surface-averaged heat flux between 30°S and 30°N . For $Q \leq 0$, the solid mass fraction is zero since inward heat flux at any point is assumed to cause melting. For $0 < Q < \bar{Q}_{ic}$, the solid mass fraction varies linearly with Q/\bar{Q}_{ic} . The mean solid mass fraction in the eastern hemisphere is subsequently determined by averaging the mass fraction over all points between 30°S and 30°N . The hemispherical solid mass fractions are related

to the respective mean ICB heat fluxes by

$$\frac{x_{s,e}}{x_{s,w}} = \frac{E_{avg}}{W_{avg}}, \quad (7)$$

which gives the solid mass fraction in the west, $x_{s,w}$.

The density of the solid phase of iron over the ICB, $\rho_s = 12704 \text{ kg m}^{-3}$, is taken from the reference model AK135 (Kennett et al., 1995). The density of liquid iron is given the value $\rho_l = \rho_s - \Delta$, where $\Delta = 240 \text{ kg m}^{-3}$ (Alfè et al., 2002). While it has been argued that the density jump at the ICB might be near 300 kg m^{-3} (Irving et al., 2018; Robson and Romanowicz, 2019), the value taken in this study lies in the range $200\text{--}300 \text{ kg m}^{-3}$ (Koper and Pyle, 2004; Tkalčić et al., 2009), and is reasonable if one assumes that the change in density is mainly due to solidification rather than differences in composition between the solid and liquid phases. The mean density for either hemisphere is calculated from the densities of the two pure phases by the method of ‘Reuss averaging’ (Anderson, 1989, p. 125),

$$\rho = \frac{1}{\frac{x_s}{\rho_s} + \frac{x_l}{\rho_l}}, \quad (8)$$

where $x_l = 1 - x_s$. The mean bulk modulus K for either hemisphere is calculated by the same method, where the bulk moduli of the solid and liquid phases, K_s and K_l , are obtained from the model AK135. The body wave compressional velocity for either hemisphere is then given by

$$v_p = \sqrt{\frac{K}{\rho}}, \quad (9)$$

where the shear modulus of the mixture is ignored in the calculation of v_p (see Gubbins et al., 2008).

The difference in seismic velocity between the eastern and western hemispheres is given by

$$\Delta v_p = v_{p,e} - v_{p,w}. \quad (10)$$

Using the values of K_s and K_l from the reference model PREM (Dziewonski and Anderson, 1981) gives a lower value of Δv_p than that obtained using AK135 because the higher value of K_l in PREM lowers the velocity contrast between the solid and liquid phases.

The relative difference in freezing rate between the hemispheres is given by

$$\Delta r_f = (E_{avg} - W_{avg}) / \bar{Q}_{ic}. \quad (11)$$

Author	Reference model - V_p	ΔV_p in % (in ms^{-1})	Boundaries
Niu and Wen (2001)	PREM - 11.03 km s^{-1}	0.8 (88)	$40^\circ\text{E}, 180^\circ\text{E}$
Sun and Song (2008)	AK135 - 11.04 km s^{-1}	0.5 (55)	$40^\circ\text{E}, 160^\circ\text{E}$
Waszek and Deuss (2011)	AK135 - 11.04 km s^{-1}	1.5 (165)	$10^\circ\text{--}14^\circ\text{E}, 173^\circ\text{E}$
Burdick et al. (2019)	AK135 - 11.04 km s^{-1}	1.0 (110)	$24^\circ\text{E}, 180^\circ\text{E}$

Author	F-layer height (km)
Souriau and Poupinet (1991)	150
Kennett et al. (1995)	150
Zou et al. (2008)	350
Ohtaki and Kaneshima (2015)	230-380

Table 2: Top panel: Summary of studies listing the difference in average isotropic P-wave velocity between the quasi-eastern and quasi-western hemispheres in the outermost region of the inner core. The absolute difference between the eastern and western hemispheres (Δv_p) is calculated using the hemispherical differences in per cent and the reference velocity used in each work. The boundaries dividing the quasi-eastern and quasi-western hemispheres are also given. Bottom panel: Estimates of the F-layer height proposed by different seismic studies.

Previous studies that map the isotropic P-wave velocity at the top of the inner core report a difference of 0.5-1.5% between the two hemispheres, which translates to absolute differences of $\approx 50\text{--}160 \text{ ms}^{-1}$ (table 2). In these studies, the boundaries demarcating the eastern and western hemispheres are not located at 0° and 180° ; rather, ‘quasi-eastern’ and ‘quasi-western’ hemispheres are considered (e.g. Tanaka and Hamaguchi, 1997) based on

Sr. no.	E	q^*	Ra^T ($\times 10^6$)	Ra^C ($\times 10^9$)	Heat flux			Mass fraction		Density		Bulk modulus		Δr_f (%)	Δv_p (ms^{-1})
					E_{avg}	W_{avg}	\bar{Q}_{ic}	$x_{s,e}$	$x_{s,w}$	ρ_e	ρ_w	K_e	K_w		
a	2×10^{-6}	1	7.2	2	1.38 (1.23)	1.32 (1.13)	1.35 (1.18)	0.80 (0.71)	0.77 (0.65)	12655 (12633)	12647 (12620)	1.330 (1.325)	1.328 (1.315)	3.77 (8.42)	4 (7)
b		2	6.75	2	1.14 (0.90)	1.07 (0.77)	1.10 (0.83)	0.75 (0.63)	0.70 (0.54)	12643 (12614)	12630 (12592)	1.327 (1.320)	1.324 (1.315)	6.60 (15.57)	7 (12)
c^\dagger		7	5.75	2	1.04 (1.03)	0.83 (0.60)	0.94 (0.82)	0.73 (0.67)	0.56 (0.48)	12638 (12624)	12603 (12557)	1.326 (1.323)	1.317 (1.307)	22.64 (52.60)	21 (35)
d		7	5.75	2.75	1.39 (1.26)	1.20 (1.01)	1.30 (1.13)	0.69 (0.60)	0.60 (0.48)	12629 (12607)	12606 (12598)	1.324 (1.318)	1.318 (1.312)	14.73 (22.03)	12 (15)
e^\dagger		10	4.30	2.75	1.25 (1.21)	1.01 (0.75)	1.13 (0.98)	0.70 (0.58)	0.57 (0.35)	12631 (12602)	12599 (12549)	1.324 (1.318)	1.317 (1.305)	20.75 (46.94)	17 (28)
f		10	4.30	3.5	1.89 (1.80)	1.78 (1.60)	1.84 (1.75)	0.75 (0.65)	0.71 (0.58)	12643 (12619)	12633 (12602)	1.327 (1.322)	1.325 (1.317)	5.98 (11.76)	6 (11)
g		10	4.30	4.25	2.87 (2.60)	2.75 (2.30)	2.81 (2.45)	0.83 (0.74)	0.80 (0.65)	12663 (12641)	12654 (12620)	1.332 (1.327)	1.330 (1.322)	4.27 (12.24)	4 (11)
h	1×10^{-5}	10	1.12	0.9	0.56 (0.26)	0.46 (0.15)	0.51 (0.20)	0.70 (0.50)	0.58 (0.29)	12631 (12585)	12601 (12534)	1.324 (1.313)	1.317 (1.301)	19.61 (52.31)	16 (28)
i		15	0.87	1.05	0.39 (0.09)	0.33 (0.06)	0.36 (0.075)	0.67 (0.61)	0.36 (0.41)	12624 (12609)	12599 (12560)	1.322 (1.319)	1.316 (1.307)	16.67 (40.00)	14 (26)

Table 3: Differences in average freezing rate Δr_f (per cent) and P-wave velocity difference Δv_p (m s^{-1}) between the eastern and western hemispheres evaluated between 30°S and 30°N of the ICB. The values in the brackets are those calculated for the equator. The regime of stable convection beneath Asia and time-varying convection beneath the Atlantic is considered in all runs. Here, $x_{s,e}$ and $x_{s,w}$ are the solid mass fractions in the eastern and western hemispheres of the inner core, ρ_e and ρ_w are the respective mean densities and K_e and K_w are the respective mean bulk moduli. The superscript \dagger denotes the parameters for which the reversal of heat flux and Δr_f , Δv_p are the highest among the runs performed for that q^* . The dynamo parameters are $Pr = 0.1$, $Sc = 1$, $Pm = 1$, $E = 2 \times 10^{-6}$ for (a)–(g) and $Pr = 0.1$, $Sc = 1$, $Pm = 1$, $E = 1 \times 10^{-5}$ for (h)–(i).

the magnitudes of the P-wave velocity relative to its reference value prescribed by PREM (Dziewonski and Anderson, 1981) or AK135 (Kennett et al., 1995). Table 3 gives the east–west differences in the freezing rate and isotropic P-wave velocity at the ICB using the hemispherical heat fluxes in the dynamo simulations. The differences (Δr_f in per cent and Δv_p in m s^{-1}) are estimated for the conventional hemispherical boundaries at $[0^\circ, 180^\circ]$ and latitudes $[30^\circ\text{S}, 30^\circ\text{N}]$. For q^* of $O(10)$, the values of Δv_p at the equator, given within brackets, do not reach the the lower bound of the observed variation (table 2) but are of the same order of magnitude. Since the dynamo model has no reference seismic velocity, it

would not be logical to estimate the east–west differences for skewed boundaries between the hemispheres. Nevertheless, when the averaging in (7) is performed over a truncated eastern hemisphere, the hemispherical differences increase because part of the region with negative heat flux in the Pacific at q^* of $O(10)$ now lies in the quasi-western hemisphere. Consequently, this lowers W_{avg} relative to E_{avg} , resulting in an increased contrast between the two hemispheres. For example, a variation of $\Delta v_p \approx 50 \text{ m s}^{-1}$ is obtained for $q^* = 10$ with the quasi-eastern boundaries $[40^\circ\text{E}, 160^\circ\text{E}]$. This is near the lower bound of the observed variation.

The values of Δr_f and Δv_p at q^* of $O(1)$ and $O(10)$ suggest that the CMB must have a heterogeneity q^* of at least $O(10)$.

2.4. Height of the melt-induced stratified layer at the base of the outer core

A stably stratified layer at the base of the Earth’s core (Souriau and Poupinet, 1991; Zou et al., 2008; Ohtaki and Kaneshima, 2015), also known as the F-layer, can be explained by localized melting of the inner core (Gubbins et al., 2008, 2011). Here, outer core convection causes heat flow into the inner core primarily beneath the Pacific and to a lesser extent beneath Africa, which in turn produces the melt that feeds the layer. The shallow water approximation for an incompressible Boussinesq fluid (Deguen et al., 2014) subject to buoyant forcing and magnetic damping provides a useful model for the F-layer.

The conservation of mass in a layer where the density decreases linearly from bottom to top is given by

$$\frac{\partial h}{\partial t} + \nabla \cdot (\mathbf{u}h) = 2w, \quad (12)$$

where \mathbf{u} is the horizontal velocity averaged over the layer height h , w is the volume flux per unit area into the layer from the inner core and the mean variation in density across the layer is half the difference in density between the top and bottom. The ICB heat flux variation in figure 3 (c) suggests that w would take the approximate form $w_0 \cos 2\phi$, where the peak volume flux density $w_0 \sim \kappa_T/h_0$ from the steady-state heat equation, ϕ is the

longitudinal separation from the point of peak inward heat flux and h_0 is the peak layer height.

The equation of motion in the layer is given by

$$\rho \left(\frac{\partial \mathbf{u}}{\partial t} + 2\boldsymbol{\Omega} \times \mathbf{u} \right) = -g\delta\rho\nabla h + \mathbf{j} \times \mathbf{B}, \quad (13)$$

where $\boldsymbol{\Omega}$ is the angular velocity of rotation, \mathbf{j} is the induced electric current density, ρ is the mean density of the layer and $\delta\rho$ is the variation of density across the layer. Both nonlinear inertial and viscous forces are small relative to the Coriolis force in the rapidly rotating core; that said, since the east–west variation is thought to be maximum near the equator (figure 2), the analysis is confined to the equator where the Coriolis force does not enter the force balance. In the steady state, the lateral buoyancy is balanced by the Lorentz force in the layer. Given that density disturbances of length scale ~ 10 km, of magnetic Reynolds number $Rm \sim 1$ –10, can generate the field (Sreenivasan and Maurya, 2021), the estimation of the Lorentz force in the low- Rm approximation is appropriate (Moffatt and Loper, 1994). Since the s and ϕ (in cylindrical coordinates s, ϕ, z) magnetic fields are zero at the equator, the ambient field \mathbf{B} is approximated by a time and azimuthally averaged z field at the equator in the saturated dynamo. We obtain (Sreenivasan and Alboussière, 2000)

$$\mathbf{j} \times \mathbf{B} \sim \sigma B_z^2 \ell^* \mathbf{u}, \quad (14)$$

where the curl of Ohm’s law is used to estimate the electric current, σ is the electrical conductivity and $\ell^* = \ell_\perp / \ell_\parallel$ is the ratio of length scales perpendicular and parallel to the ambient field direction.

In the steady state, equations (12) and (13) may now be combined to obtain the following dimensionless equation for the layer height at the equator:

$$\nabla^2 h^{*2} = -\frac{4\ell^* B_z^{*2}}{h_0^* Ra_H} \cos 2\phi. \quad (15)$$

where h^* and B_z^* denote the layer height and field intensity scaled as in the dynamo model and the modified horizontal Rayleigh number $Ra_H = g\alpha\Delta Q_H L^2 / 2\Omega \kappa_T$ is based on the

average difference in equatorial ICB heat flux between Asia, where the model suggests predominant freezing, and the Pacific, where the model suggests predominant melting. The Asian heat flux is evaluated over [30°E, 120°E] and the Pacific heat flux over [120°E, 150°W], consistent with the longitudinal separation of approximately 90° between the peak and trough of the equatorial heat flux at high q^* (figure 3(c)).

Equation (15) is solved subject to the conditions $h^2 = h_0^2$ at $\phi = 0$ and $h^2 = 0$ at $\phi = \pi/2$, indicating that the layer height goes to zero at the point of peak freezing. The F-layer height is then given by

$$h^{*2} \sim h_0^{*2} + \frac{B_z^{*2} \ell^* r_i^{*2} (\cos 2\phi - 1)}{Ra_H h_0^*}, \quad (16)$$

where

$$h_0^* \sim \left(\frac{2r_i^{*2} \ell^* B_z^{*2}}{Ra_H} \right)^{1/3} \quad (17)$$

gives the maximum height of the layer. For flow length scales $\ell_\perp \sim 10$ km within the F-layer where $\ell_\parallel \sim 100$ km, the ratio $\ell^* \sim 0.1$.

The mean scaled height \bar{h}^* given in table 4 is obtained from the distribution of h^* over the surface of the inner core. A layer height $\bar{h} \approx 200$ km, obtained for $q^* = 10$, lies within the range of 150–400 km proposed by earlier studies (see table 2). On the other hand, the mean height of a viscously damped layer (Deguen et al., 2014) is ≈ 100 km. Although the present analysis is based on orders of magnitude, it supports the existence of a melt-induced and magnetically damped layer at the base of the outer core.

2.5. High-latitude magnetic flux at the CMB

For the dynamo with $Ra^T = 4.3 \times 10^6$ ($\approx Ra_{cr}^T$), $Ra^C = 2.75 \times 10^9$ ($\approx 180 \times Ra_{cr}^C$) and $q^* = 10$, a long-lived pair of high-latitude flux lobes exist in the East and highly time-varying lobes are found in the West. While the coherent downwelling beneath Asia concentrates quasi-stationary magnetic flux, the time-varying convection beneath America produces flux patches which are relatively unstable. The time-averaged B_r at the CMB is shown in figure 4(b). The pair of lobes in the Western hemisphere appear fragmented on

S. no.	E	q^*	Ra^T ($\times 10^6$)	Ra^C ($\times 10^9$)	ΔQ_H	Ra_H	B_z^{*2}	\bar{h}^*	\bar{h} (km)
a	2×10^{-6}	7	5.75	2	1.67	12.47	0.42	0.082	185
b		7	5.75	2.75	1.94	14.48	0.52	0.083	188
c		10	4.30	2.75	2.23	12.45	0.50	0.086	194
d		10	4.30	3.5	2.91	16.25	0.66	0.087	196
e		10	4.30	4.25	2.48	13.84	0.82	0.098	221
f	1×10^{-5}	10	1.12	0.9	1.51	10.78	0.58	0.095	215
g		15	0.87	1.05	2.40	13.56	0.64	0.091	205

Table 4: Average height of the F-layer scaled by the depth of the outer core (\bar{h}^*) in the dynamo simulations for varying q^* in the regime of coherent convection beneath Asia and time-varying convection beneath America. The common parameters in the simulations are $Pr = 0.1$, $Sc = 1$ and $Pm = 1$. The thermal Rayleigh number Ra^T is set to its critical value. The modified horizontal Rayleigh number Ra_H is based on ΔQ_H , the difference in measured average heat flux between the Asian and Pacific sectors of the ICB at the equator.

time average due to their variable locations at different times. There are also times when convection beneath the Atlantic is stable and gives an approximately $m = 2$ pattern of magnetic flux lobes. The location of the flux lobes is in fair agreement with that at the Earth’s CMB (figure 4(a)), where the magnetic field is obtained from the CALS10k.2 model compiled from archaeomagnetic and paleomagnetic data for the past 10000 years (Constable et al., 2016). The time average is for the period 1590–1990 AD. While Earth-like fields are not produced for large CMB heterogeneity in weakly rotating dynamos with $E \sim 10^{-4}$ (Driscoll, 2015), the rapidly rotating dynamos with $E \sim 10^{-6}$ considered here can reproduce Earth-like fields even for q^* of $O(10)$.

Figures 4 (c) & (d) show the longitudinal positions of the peak magnetic flux in the Northern hemisphere lobes. The east–west variability in the dynamo simulation is compared with that of the archeomagnetic field model CALS10k.2 (Constable et al., 2016) from 4000 BC to 1990 AD and the CHAOS-7.12 model from 1990 to 2020 (Finlay et al.,

2020). The solid lines in figure 4 (c) show the historical peaks of the magnetic flux lobes for the past 6000 years. In the past 3000 years, the western hemisphere lobes have been more mobile than their eastern hemisphere counterparts – while the Canadian flux lobe moved between 50°W to 100°W , the Siberian lobe moved between 90°E and 120°E . The dynamo simulation at $Ra^C = 2.75 \times 10^9$ ($\approx 180 \times Ra_{cr}^C$) and $q^* = 10$ shows lower longitudinal variations of the Siberian lobe relative to the Canadian lobe (figure 4 (d)), consistent with that in Earth’s field. The Canadian lobe moves between 65°W and 130°W and occasionally disappears while the Siberian lobe moves between 90°E and 130°E .

3. Discussion

The study shows that a thermally heterogeneous CMB induces a substantial variation of heat flux at the ICB through the medium of outer core convection. A two-component convective dynamo model, where thermal convection is near critical and compositional convection is strongly supercritical, produces inner core heterogeneity in the strongly driven regime of present-day Earth. The temperature profile that models secular cooling ensures that the CMB thermal heterogeneity is transmitted to the ICB. The precise distribution of heat flux at the ICB, on the other hand, is determined by the strength of compositional buoyancy, measured by Ra^C . High values of Ra^C ($\sim 10^2 \times Ra_{cr}^C$ in this study) produces a long-lived downwelling beneath Asia and time-varying convection beneath America, which in turn results in a higher average freezing rate and seismic P-wave velocity in the eastern hemisphere relative to the western hemisphere. Since laboratory models of core convection (Sahoo and Sreenivasan, 2020b) indicate that the CMB heterogeneity would penetrate as far as the ICB when convection originates in close proximity to the boundary anomalies, the success of the two-component model rests on the temperature profile rather than the ratio of thermal to compositional diffusivities.

For moderate CMB heterogeneity, measured by q^* of $O(1)$, the ICB heat flux pattern is approximately two-fold, with approximately equal peaks of heat flux in the east and west and no inward (negative) heat flux (figure 3(b)). For a relatively large CMB heterogeneity

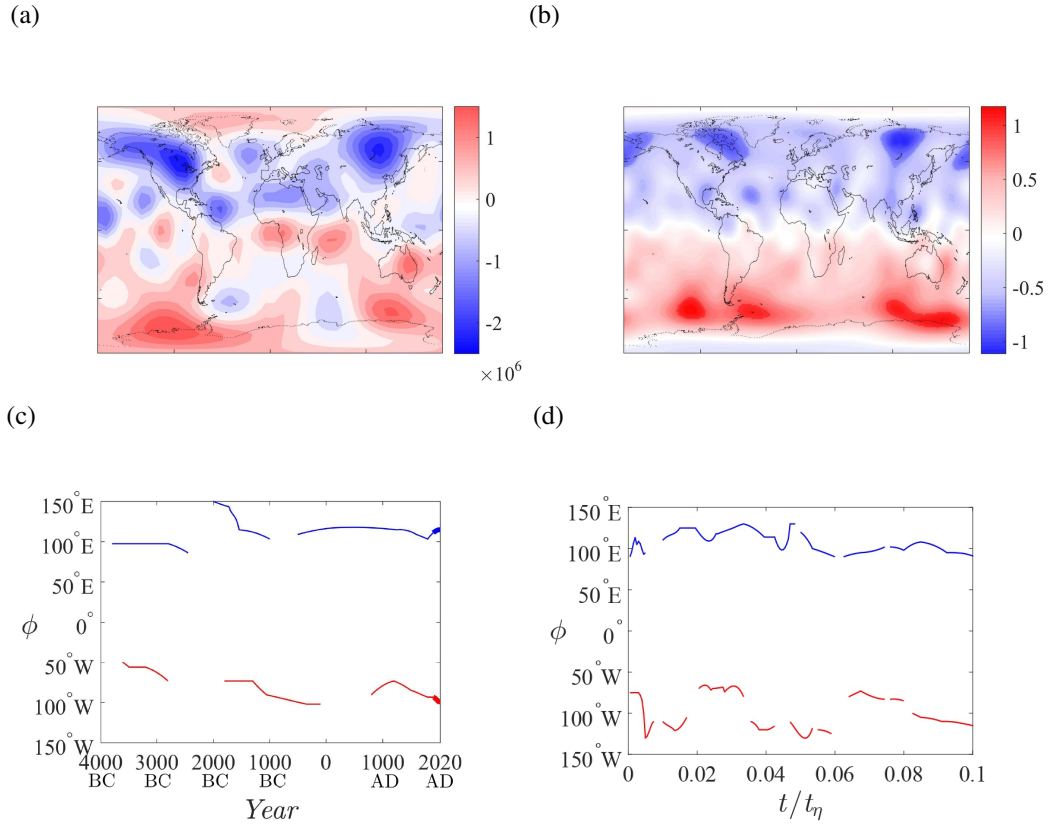


Figure 4: Time-averaged B_r at the CMB for (a) CALS10k.2 model for the years 1590-1990 AD and in (b) B_r in the dynamo. (c), (d) Time series of the longitude of the peak value of the high-latitude flux patches in the Northern hemisphere for the CALS10k.2+ CHAOS-7.12 field model and the dynamo respectively. The dynamo parameters are $Ra^T = 4.30 \times 10^6$ ($\approx Ra_{cr}^T$), $Ra^C = 2.75 \times 10^9$ ($\approx 180 \times Ra_{cr}^C$), $q^* = 10$, with $Pr = 0.1$, $Sc = 1$, $Pm = 1$, and $E = 2 \times 10^{-6}$. The field at the CMB is plotted for the spherical harmonic degree range $1 \leq l \leq 10$.

of q^* of $O(10)$, heat flux peak beneath Asia dominates that beneath America, and regions of inward heat flux develop strongly beneath the Pacific and weakly beneath Africa (figure 3(c)). This two-fold pattern with dominant heat flux beneath Asia is supported by observations (e.g. Cormier and Attanayake, 2013; Tkalčić et al., 2024). The departure from the hemispherical ($m = 1$) heterogeneity points towards the influence of the CMB on the freezing rate heterogeneity of the inner core. Increasing q^* to higher values necessitates a higher Ra^C to obtain comparable average heat flux differences at the ICB. Increasing Ra^C to high values for a given q^* causes the inward heat flux to weaken and the heat flux averages in the hemispheres to equalize again (figure 3(d)) as the convection in the eastern hemisphere also becomes time-varying. The values of $(q^*, Ra^C/Ra_{cr}^C)$ proposed in this study are conservative lower bounds for Earth. An upper bound of Ra^C/Ra_{cr}^C would be $O(10^3)$, at which strong anticyclonic polar vortices must exist below the threshold for polarity reversals in the inertia-less core (Majumder and Sreenivasan, 2023). This may in turn place an upper bound for q^* .

Many studies (Loper and Roberts, 1977; Wong et al., 2018) describe the F-layer at the base of the outer core as a two-phase, two-component slurry, where solid particles freeze throughout the layer and sink under gravity while the light elements migrate to the outer core without disturbing the layer. This study, on the other hand, considers the liquid produced by localized melting of the inner core to be the source of the F-layer. Although preferential melting in one hemisphere can result from convective translation of the inner core (Alboussiere et al., 2010; Deguen et al., 2014), here we propose that the lower mantle, through outer core convection, causes regional melting of the inner core, in line with Gubbins et al. (2011). The liquid produced by melting then spreads over the surface of the inner core. Since the magnetic damping of this lateral flow happens on a shorter time scale than viscous damping, the build-up of melt over regions of negative heat flux would be higher in the presence of the magnetic field. Thus, in the steady state, larger layer heights $\bar{h} \sim 200$ km are realizable with magnetic damping than with viscous damping.

The parameter space of $(q^*, Ra^C/Ra_{cr}^C)$ that gives long-lived convection in the east and

time-varying convection in the west satisfies multiple observational constraints. First, the variability of high-latitude magnetic flux in the east is markedly lower than that in the west. Second, the average seismic velocity at the top of the inner core is higher in the east than that in the west, with the peak velocity beneath equatorial East Asia. Finally, the stratified layer at the base of the outer core, which is fed by the mass flux from regional melting of the inner core and magnetically damped, attains a steady-state height of ~ 200 km. All of the above factors indicate that the lower mantle has a dominant effect on inner core heterogeneity.

Acknowledgements

This study was supported by Research Grant CRG/2021/002486 awarded by the Science and Engineering Research Board (India). The computations were performed on *Param Pravega*, the supercomputer at the Indian Institute of Science, Bangalore.

Appendix A. Dynamo driven by one-component convection

The non-dimensional MHD equations for the velocity \mathbf{u} , magnetic field \mathbf{B} and temperature T are given by

$$\frac{E}{Pm} \left(\frac{\partial \mathbf{u}}{\partial t} + (\nabla \times \mathbf{u}) \times \mathbf{u} \right) + \hat{\mathbf{z}} \times \mathbf{u} = -\nabla p^* + (\nabla \times \mathbf{B}) \times \mathbf{B} + PmPr^{-1}ERaT\mathbf{r} + E\nabla^2\mathbf{u}, \quad (\text{A.1})$$

$$\frac{\partial T}{\partial t} + (\mathbf{u} \cdot \nabla)T = PmPr^{-1}\nabla^2T, \quad (\text{A.2})$$

$$\frac{\partial \mathbf{B}}{\partial t} = \nabla \times (\mathbf{u} \times \mathbf{B}) + \nabla^2\mathbf{B}, \quad (\text{A.3})$$

$$\nabla \cdot \mathbf{u} = \nabla \cdot \mathbf{B} = 0, \quad (\text{A.4})$$

where $p^* = p + \frac{1}{2}EPm^{-1}|\mathbf{u}^2|$ is the modified pressure and $\hat{\mathbf{z}} = [\cos \theta, -\sin \theta, 0]$. The dimensionless parameters in the above equations are as defined in Section 2.1 of the paper.

The basic state temperature profile is obtained by solving

$$PmPr^{-1} \frac{1}{r^2} \frac{\partial}{\partial r} \left(r^2 \frac{\partial T_0}{\partial r} \right) - S_i = 0, \quad (\text{A.5})$$

which gives

$$T_0 = PrPm^{-1} \frac{S_i r^2}{6} + \frac{C_1}{r} + C_2. \quad (\text{A.6})$$

The boundary conditions are chosen as

$$T_0 = 0 \quad \text{at } r = r_i, \quad (\text{A.7})$$

$$\frac{\partial T_0}{\partial r} = -0.01 \quad \text{at } r = r_o. \quad (\text{A.8})$$

Using $S_i = 1$ and $PmPr^{-1} = 1$, we obtain

$$T_0 = \frac{r^2}{6} + \frac{1.236}{r} - 4.32, \quad (\text{A.9})$$

which is the combination of basal heating and a heat sink (Sreenivasan and Gubbins, 2008).

References

- T. Alboussiere, R. Deguen, and M. Melzani. Melting-induced stratification above the Earth's inner core due to convective translation. *Nature*, 466(7307):744–747, 2010.
- D. Alfè, M.J. Gillan, and G.D. Price. Composition and temperature of the Earth's core constrained by combining ab initio calculations and seismic data. *Earth Planet. Sci. Lett.*, 195(1-2):91–98, 2002.
- D.L. Anderson. *Theory of the Earth*. Blackwell Scientific Publications, 1989.
- J. Aubert, H. Amit, G. Hulot, and P. Olson. Thermochemical flows couple the Earth's inner core growth to mantle heterogeneity. *Nature*, 454(7205):758–761, 2008.

- S. Burdick, L. Waszek, and V. Lekić. Seismic tomography of the uppermost inner core. *Earth Planet. Sci. Lett.*, 528:115789, 2019.
- C. Constable, M. Korte, and S. Panovska. Persistent high paleosecular variation activity in southern hemisphere for at least 10 000 years. *Earth Planet. Sci. Lett.*, 453:78–86, 2016.
- V.F. Cormier and J. Attanayake. Earth’s solid inner core: Seismic implications of freezing and melting. *J. Earth Sci.*, 24(5):683–698, 2013.
- V.F. Cormier, M.I. Bergman, and P. Olson. *Earth’s core: geophysics of a planet’s deepest interior*. Elsevier, 2021.
- C.J. Davies and J.E. Mound. Mantle-induced temperature anomalies do not reach the inner core boundary. *Geophys. J. Int.*, 219(Supplement_1):S21–S32, 2019.
- R. Deguen, P. Olson, and E. Reynolds. F-layer formation in the outer core with asymmetric inner core growth. *C. R. - Geosci.*, 346(5-6):101–109, 2014.
- P.E. Driscoll. Testing the dynamic coupling of the core-mantle and inner core boundaries. *J. Geophys. Res. Solid Earth*, 120, 2015. doi: 10.1002/2014JB011682.
- A.M. Dziewonski and D.L. Anderson. Preliminary reference Earth model. *Phys. Earth Planet. Inter.*, 25(4):297–356, 1981.
- C.C. Finlay, C. Kloss, N. Olsen, M.D. Hammer, L. Toffner-Clausen, A. Grayver, and A. Kuvshinov. The CHAOS-7 geomagnetic field model and observed changes in the South Atlantic Anomaly. *Earth Planets Space*, 72(1):1–31, 2020.
- D. Gubbins. The Rayleigh number for convection in the Earth’s core. *Phys. Earth Planet. Inter.*, 128(1-4):3–12, 2001.
- D. Gubbins, A.P. Willis, and B. Sreenivasan. Correlation of Earth’s magnetic field with lower mantle thermal and seismic structure. *Phys. Earth Planet. Inter.*, 162(3-4):256–260, 2007.

- D. Gubbins, G. Masters, and F. Nimmo. A thermochemical boundary layer at the base of Earth's outer core and independent estimate of core heat flux. *Geophys. J. Int.*, 174(3):1007–1018, 2008.
- D. Gubbins, B. Sreenivasan, J. Mound, and S. Rost. Melting of the Earth's inner core. *Nature*, 473(7347):361–363, 2011.
- J. Irving, S. Cottaar, and V. Lekić. Seismically determined elastic parameters for Earth's outer core. *Sci. Adv.*, 4(6):eaar2538, 2018.
- A. Jackson, A.R.T. Jonkers, and M.R. Walker. Four centuries of geomagnetic secular variation from historical records. *Philos. Trans. Royal Soc. A*, 358(1768):957–990, 2000.
- B. Kennett, E.R. Engdahl, and R. Buland. Constraints on seismic velocities in the Earth from traveltimes. *Geophys. J. Int.*, 122(1):108–124, 1995.
- K.D. Koper and M.L. Pyle. Observations of PKiKP/PcP amplitude ratios and implications for earth structure at the boundaries of the liquid core. *J. Geophys. Res. Solid Earth*, 109(B3), 2004.
- D. E. Loper and P. H. Roberts. On the motion of an iron-alloy core containing a slurry: I. General theory. *Geophys. Astrophys. Fluid Dyn.*, 9(1):289–321, 1977.
- D. Majumder and B. Sreenivasan. The role of magnetic waves in tangent cylinder convection. *Phys. Earth Planet. Inter.*, 344:107105, 2023.
- A. Manglik, J. Wicht, and U.R. Christensen. A dynamo model with double diffusive convection for Mercury's core. *Earth Planet. Sci. Lett.*, 289(3-4):619–628, 2010.
- G. Masters, G. Laske, H. Bolton, and A. Dziewonski. The relative behavior of shear velocity, bulk sound speed, and compressional velocity in the mantle: Implications for chemical and thermal structure. *Geophys. Monogr. Ser.*, 117:63–87, 2000.

- H. K. Moffatt and D. E. Loper. The magnetostrophic rise of a buoyant parcel in the Earth's core. *Geophys. J. Int.*, 117:394–402, 1994.
- J. Mound and C.J. Davies. Longitudinal structure of Earth's magnetic field controlled by lower mantle heat flow. *Nat. Geosci.*, pages 1–6, 2023.
- J. Mound, C. Davies, S. Rost, and J. Aurnou. Regional stratification at the top of Earth's core due to core–mantle boundary heat flux variations. *Nat. Geosci.*, 12(7):575–580, 2019.
- F. Niu and L. Wen. Hemispherical variations in seismic velocity at the top of the Earth's inner core. *Nature*, 410(6832):1081–1084, 2001.
- T. Ohtaki and S. Kaneshima. Independent estimate of velocity structure of Earth's lowermost outer core beneath the northeast Pacific from PKiKP- PKPbc differential traveltimes and dispersion in PKPbc. *J. Geophys. Res. Solid Earth*, 120(11):7572–7586, 2015.
- T. Ohtaki, S. Kaneshima, and K. Kanjo. Seismic structure near the inner core boundary in the south polar region. *J. Geophys. Res. Solid Earth*, 117(B3), 2012.
- P. Olson and H. Amit. Mantle superplumes induce geomagnetic superchrons. *Front. Earth Sci.*, 3:38, 2015.
- P. Olson, M. Landeau, and E. Reynolds. Outer core stratification from the high latitude structure of the geomagnetic field. *Front. Earth Sci.*, 6:140, 2018.
- A. Robson and B. Romanowicz. New normal mode constraints on bulk inner core velocities and density. *Phys. Earth Planet. Inter.*, 295:106310, 2019.
- S. Sahoo and B. Sreenivasan. Response of Earth's magnetic field to large lower mantle heterogeneity. *Earth Planet. Sci. Lett.*, 549:116507, 2020a.
- S. Sahoo and B. Sreenivasan. Convection in a rapidly rotating cylindrical annulus with laterally varying boundary heat flux. *J. Fluid Mech.*, 883:A1, 2020b.

- A. Souriau and G. Poupinet. The velocity profile at the base of the liquid core from PKP (BC+ Cdiff) data: an argument in favour of radial inhomogeneity. *Geophys. Res. Lett.*, 18(11):2023–2026, 1991.
- B. Sreenivasan and T. Alboussière. Evolution of a vortex in a magnetic field. *Eur. J. Mech. B - Fluids*, 19:403–421, 2000.
- B. Sreenivasan and D. Gubbins. Dynamos with weakly convecting outer layers: implications for core-mantle boundary interaction. *Geophys. Astrophys. Fluid Dyn.*, 102(4):395–407, 2008.
- B. Sreenivasan and G. Maurya. Evolution of forced magnetohydrodynamic waves in a stratified fluid. *J. Fluid Mech.*, 922:A32, 2021.
- X. Sun and X. Song. Tomographic inversion for three-dimensional anisotropy of Earth’s inner core. *Phys. Earth Planet. Inter.*, 167(1-2):53–70, 2008.
- F. Takahashi, H. Tsunakawa, M. Matsushima, N. Mochizuki, and Y. Honkura. Effects of thermally heterogeneous structure in the lowermost mantle on the geomagnetic field strength. *Earth Planet. Sci. Lett.*, 272(3-4):738–746, 2008.
- S. Tanaka and H. Hamaguchi. Degree one heterogeneity and hemispherical variation of anisotropy in the inner core from PKP (BC)–PKP (DF) times. *J. Geophys. Res. Solid Earth*, 102(B2):2925–2938, 1997.
- H. Tkalčić, B.L.N. Kennett, and V.F. Cormier. On the inner–outer core density contrast from PKiKP/PcP amplitude ratios and uncertainties caused by seismic noise. *Geophys. J. Int.*, 179(1):425–443, 2009.
- H. Tkalčić, A.B. Belonoshko, J.B. Muir, M. Mattesini, L. Moresi, and L. Waszek. Imaging the top of the Earth’s inner core: a present-day flow model. *Sci. Rep.*, 14(1):8999, 2024.

- T. H. Torsvik, M. A. Smethurst, K. Burke, and B. Steinberger. Large igneous provinces generated from the margins of the large low-velocity provinces in the deep mantle. *Geophys. J. Int.*, 167(3):1447–1460, 2006.
- L. Waszek and A. Deuss. Distinct layering in the hemispherical seismic velocity structure of Earth’s upper inner core. *J. Geophys. Res. Solid Earth*, 116(B12), 2011.
- A.P. Willis, B. Sreenivasan, and D. Gubbins. Thermal core–mantle interaction: exploring regimes for ‘locked’ dynamo action. *Phys. Earth Planet. Inter.*, 165(1-2):83–92, 2007.
- J. Wong, C. J. Davies, and C. A. Jones. A Boussinesq slurry model of the F-layer at the base of Earth’s outer core. *Geophys. J. Int.*, 214(3):2236–2249, 2018.
- Z. Zou, K. D. Koper, and V. F. Cormier. The structure of the base of the outer core inferred from seismic waves diffracted around the inner core. *J. Geophys. Res. Solid Earth*, 113(B5), 2008.